J Adv Ceram

Research Article

Low dielectric loss in vanadium-based zircon ceramics via high-entropy strategy

Yuheng Zhang[1], Huaicheng Xiang[1,2,✉], Xiaoyu Wu[1], Yang Zhou[1], Ying Tang[1,2], Liang Fang[2,✉]

Cite this article: Zhang Y, Xiang H, Wu X, et al. *J Adv Ceram* 2025, **14**(1): 9221012. https://doi.org/10.26599/JAC.2024.9221012

ABSTRACT: Zircon ceramics have potential applications in next-generation wireless communication because of their low permittivity and adjustable temperature coefficient at microwave frequencies. However, the vast challenge of realizing ultralow dielectric loss still exists. Here, we propose a high-entropy strategy to enhance the bonding of the A-site dodecahedron in zircon and design $(Nd_{0.2}Eu_{0.2}Y_{0.2}Ho_{0.2}Yb_{0.2})VO_4$ ceramics with a high quality factor (high $Q \times f$, that is, low dielectric loss). The $(Nd_{0.2}Eu_{0.2}Y_{0.2}Ho_{0.2}Yb_{0.2})VO_4$ high-entropy ceramics, which belong to the tetragonal zircon structure with the $I4_1/amd$ space group, exhibit a low relative permittivity (ε_r = 11.55), a negative temperature coefficient of resonant frequency (τ_f = −37.3 ppm/°C), and a high $Q \times f$ of 76,400 GHz (at 12.31 GHz). The high $Q \times f$ value can be attributed to the high chemical bond strength and structural stability. Furthermore, the relationship between the crystal structure and the microwave dielectric properties of $(Nd_{0.2}Eu_{0.2}Y_{0.2}Ho_{0.2}Yb_{0.2})VO_4$ high-entropy ceramics was analyzed through high resolution transmission electron microscopy (HRTEM), Raman spectroscopy, far-infrared reflection spectroscopy, and chemical bond theory. This work provides an effective avenue for designing microwave dielectric materials with low loss to meet the demands of passive components.

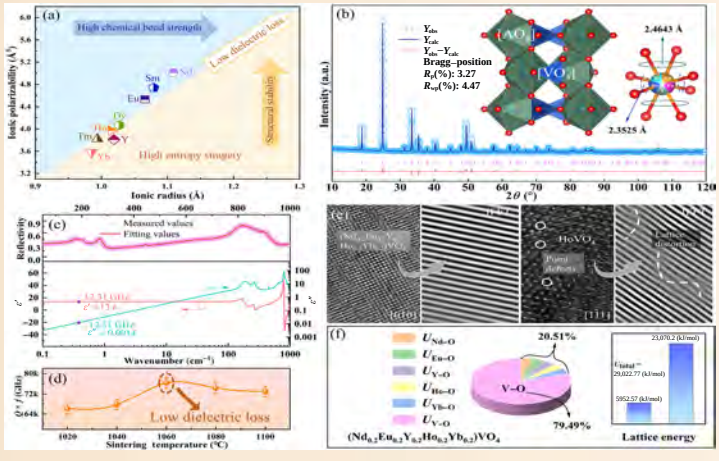

KEYWORDS: high-entropy ceramics; vanadium-based zircon; microwave dielectric properties; low dielectric loss; chemical bond characteristics

1 Introduction

Microwave dielectric ceramics, as the core component of the fabrication of passive electronic devices, are widely used in numerous fields, such as filters, dielectric antennas, and microwave communications [1–3]. For high-frequency communication, microwave dielectric ceramics with low relative permittivity (ε_r) are preferable because of their ability to decrease signal latency and facilitate the manufacturing of passive components. Additionally, microwave dielectric ceramics that are ideal for making passive components should have a temperature coefficient of resonant frequency (τ_f) near zero, which is feasible, and a high quality factor (high $Q \times f$, that is, low dielectric loss $\tan\delta = 1/Q$) [4,5]. Microwave dielectric ceramics with various structures have been prepared, including perovskite, corundum, garnet, spinel, olivine, cordierite, zircon, yellow melilite, and tungsten bronze [6–13]. Researchers have concentrated on vanadium-based zircon ceramics (Fig. 1(a)) because of their low ε_r (9.9–32.5), low sintering temperature (950–1240 °C), and ability to change τ_f from negative to positive ((−52.9)–(+80.0) ppm/°C) through ion substitution regulation, such as $(Bi_{1-x}Ce_x)VO_4$ [14] and $(Bi_{1-x}Ho_x)VO_4$ [15]. The structure of AVO_4 zircon is composed of a distorted $[AO_8]$ dodecahedron and a regular $[VO_4]$ tetrahedron, and its high dielectric loss ($Q \times f$ = 20,000–50,000 GHz) is affected mainly by the nonharmonic vibration of cations in the dodecahedron [16,17], such as $SmVO_4$ ($Q \times f$ = 38,620 GHz) and $HoVO_4$ ($Q \times f$ = 24,100 GHz).

High-entropy ceramics have attracted increasing interest because of their superior mechanical properties [18], excellent dielectric properties [19], especially high thermal stability [20], and flexible ingredient controllability [21]. The distortion effect of high-entropy ceramics is generally thought to decrease $Q \times f$, but τ_f can

[1] College of Physics and Electronic Information Engineering, Guilin University of Technology, Guilin 541004, China. [2] Guangxi Universities Key Laboratory of Non-Ferrous Metal Oxide Electronic Functional Materials and Devices, Guangxi Key Laboratory of Optical and Electronic Materials and Devices, College of Materials Science and Engineering, Guilin University of Technology, Guilin 541004, China.

✉ Corresponding authors. E-mail: H. Xiang, xianghc@glut.edu.cn; L. Fang, fanglianggl001@aliyun.com

Received: September 25, 2024; Revised: November 8, 2024; Accepted: December 1, 2024

be effectively regulated. For example, Xiang *et al.* [22] first prepared and reported high-entropy microwave dielectric ceramics with an orthorhombic olivine structure, Li $(Gd_{0.2}Ho_{0.2}Er_{0.2}Yb_{0.2}Lu_{0.2})GeO_4$, whose τ_f is close to zero (−2.9 ppm/°C), but $Q \times f$ is not prominent (29,000 GHz). Lin *et al.* [23,24] reported K_2NiF_4-structured $SrLa(Al_{0.25}Zn_{0.125}Mg_{0.125}Ti_{0.25}Ga_{0.25})O_4$ and $Sr(La_{0.2}Nd_{0.2}Sm_{0.2}Eu_{0.2}Gd_{0.2})AlO_4$ high-entropy ceramics with τ_f values of −1.7 and −6 ppm/°C, respectively. Notably, compared with those of the nonhigh-entropy ceramics $SrLaAlO_4$, their $Q \times f$ values are significantly lower. A similar phenomenon occurs in the $Mg_{1.8}(Ni_{1/5}Co_{1/5}Zn_{1/5}Cu_{1/5}Mn_{1/5})_{0.2}Al_4Si_5O_{18}$ high-entropy ceramics with a cordierite structure [25]. In the zircon structure, however, when a single ion occupies the dodecahedron at the A-site, it will cause large lattice distortion, resulting in high dielectric loss. If the A-site occupies a variety of ions to form a high-entropy effect, its dielectric loss is expected to be reduced.

On the basis of the effective ionic radius, ionic polarizability, and bond energy theory, in this work, an effective high-entropy strategy is proposed to design high-entropy ceramics $(Nd_{0.2}Eu_{0.2}Y_{0.2}Ho_{0.2}Yb_{0.2})VO_4$ with a zircon structure. As shown in Fig. 1(b), numerous rare-earth ions (Nd^{3+}, Eu^{3+}, Y^{3+}, Ho^{3+}, and Yb^{3+}) with the same valence state but different ionic radii and ionic polarizability are introduced into AVO_4 lattices to repair the distortion of the dodecahedron at the A-site to increase bonding and stabilize the crystal structure, thereby improving the $Q \times f$ value. Encouragingly, a $Q \times f$ value (76,400 GHz) more than twice as high as that of conventional zircon ceramics was achieved in $(Nd_{0.2}Eu_{0.2}Y_{0.2}Ho_{0.2}Yb_{0.2})VO_4$ high-entropy ceramics, which is the optimal performance of zircon ceramics reported to date. These findings prove that the high-entropy strategy can guide the development of new microwave dielectric ceramics with ultralow dielectric losses.

2 Experimental

$(Nd_{0.2}Eu_{0.2}Y_{0.2}Ho_{0.2}Yb_{0.2})VO_4$ high-entropy ceramics were fabricated via a conventional solid-state reaction method. Nd_2O_3, Eu_2O_3, Y_2O_3, Ho_2O_3, Yb_2O_3 (99.99%, Aladdin, USA), and NH_4VO_3 (99.95%, Aladdin, USA) were used as starting materials. The stoichiometric ratio of the raw materials was weighed, and the raw materials were ball milled at 300 r/min for 6 h via a planetary ball mill (XQM-4A, Tencan Powder, China) with alcohol as the milling medium. The mixed powders were dried and calcined at 900 °C for 4 h, followed by a second ball milling process for 6 h to obtain fine powders. Next, the calcined and ball-milled powders were mixed with a 5 wt% poly(vinyl alcohol) aqueous solution (PVA) as a binder and pressed into cylindrical samples with a thickness of 5 mm and a diameter of 10 mm under a pressure of 200 MPa. The cold-pressed samples were heated at 550 °C for 6 h to remove PVA, followed by sintering at 1020–1100 °C for 4 h.

A powder X-ray diffractometer (X'pert PRO, PANalytical, the Netherlands) was used to characterize the phase composition and crystal structure. The microstructure and elemental distribution were examined by a scanning electron microscope (SEM; S-4800, Hitachi High-Technologies, Japan). The lattice architecture was elucidated through a high-resolution transmission electron microscope (HRTEM; JEM-2100F, JEOL, Japan), complemented by selected-area electron diffraction (SAED) patterns. The analysis of local vibrational modes was conducted via a Raman spectroscope (Fisher DXR, Thermo Electron, USA). The bulk density was determined via Archimedes' drainage method. The temperature-dependent variations in ε_r and dielectric loss (tanδ) were characterized via a dielectric measurement system (DMS-300, Partulab Technologies, China). The direct current (DC) resistivity of the ceramics across a range of temperatures was assessed with a high-temperature resistivity measurement system (RMS1000I, Partulab Technologies, China). The microwave dielectric properties were evaluated via a vector network analyzer (N5230A, Agilent, USA) in TE_{011} mode via the Hakki-Coleman dielectric resonator method. The τ_f from 25 °C (T_1) to 85 °C (T_2) was calculated according to Eq. (1):

$$\tau_f = \frac{f_{T_2} - f_{T_1}}{f_{T_1} \times (T_2 - T_1)} \quad (1)$$

3 Results and discussion

Figure 2(a) presents the X-ray diffraction (XRD) patterns of the $(Nd_{0.2}Eu_{0.2}Y_{0.2}Ho_{0.2}Yb_{0.2})VO_4$ high-entropy ceramics, which were sintered at various temperatures. The diffraction peaks are attributed to a tetragonal zircon structure corresponding to the powder diffraction file (PDF) number 01-82-1973 and are associated with the $I4_1/amd$ space group. No additional diffraction peaks are observed, indicating that single-phase high-entropy ceramics can be synthesized at 1020–1100 °C. XRD data of $(Nd_{0.2}Eu_{0.2}Y_{0.2}Ho_{0.2}Yb_{0.2})VO_4$ high-entropy ceramics were analyzed via the Rietveld refinement method, and the results are displayed in Figs. 2(b)–2(f). The lattice parameters of $(Nd_{0.2}Eu_{0.2}Y_{0.2}Ho_{0.2}Yb_{0.2})VO_4$ high-entropy ceramics are presented in Table 1. The rietveld parameters, weighted profile factor (R_{wp}) =

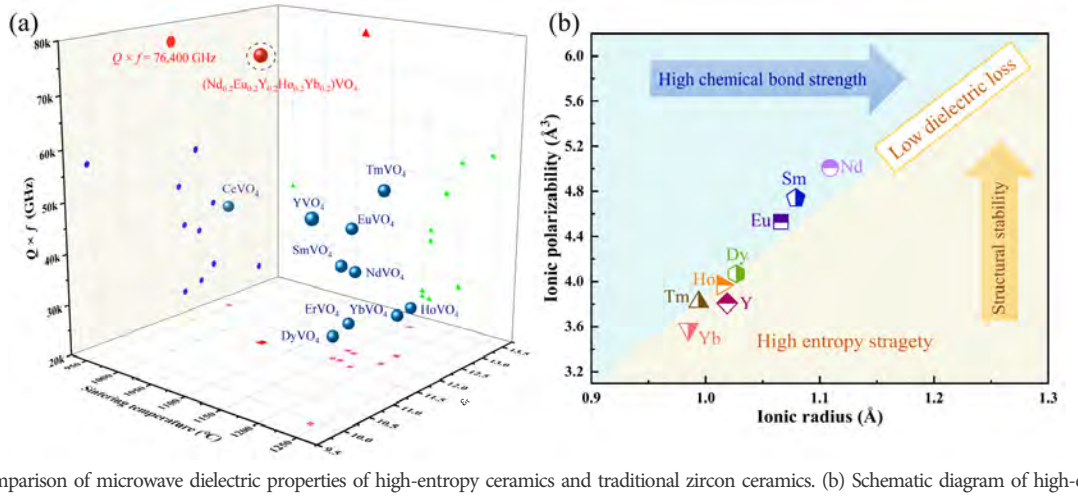

Fig. 1 (a) Comparison of microwave dielectric properties of high-entropy ceramics and traditional zircon ceramics. (b) Schematic diagram of high-entropy design strategy for enhancing bonding and stabilizing the crystal structure.

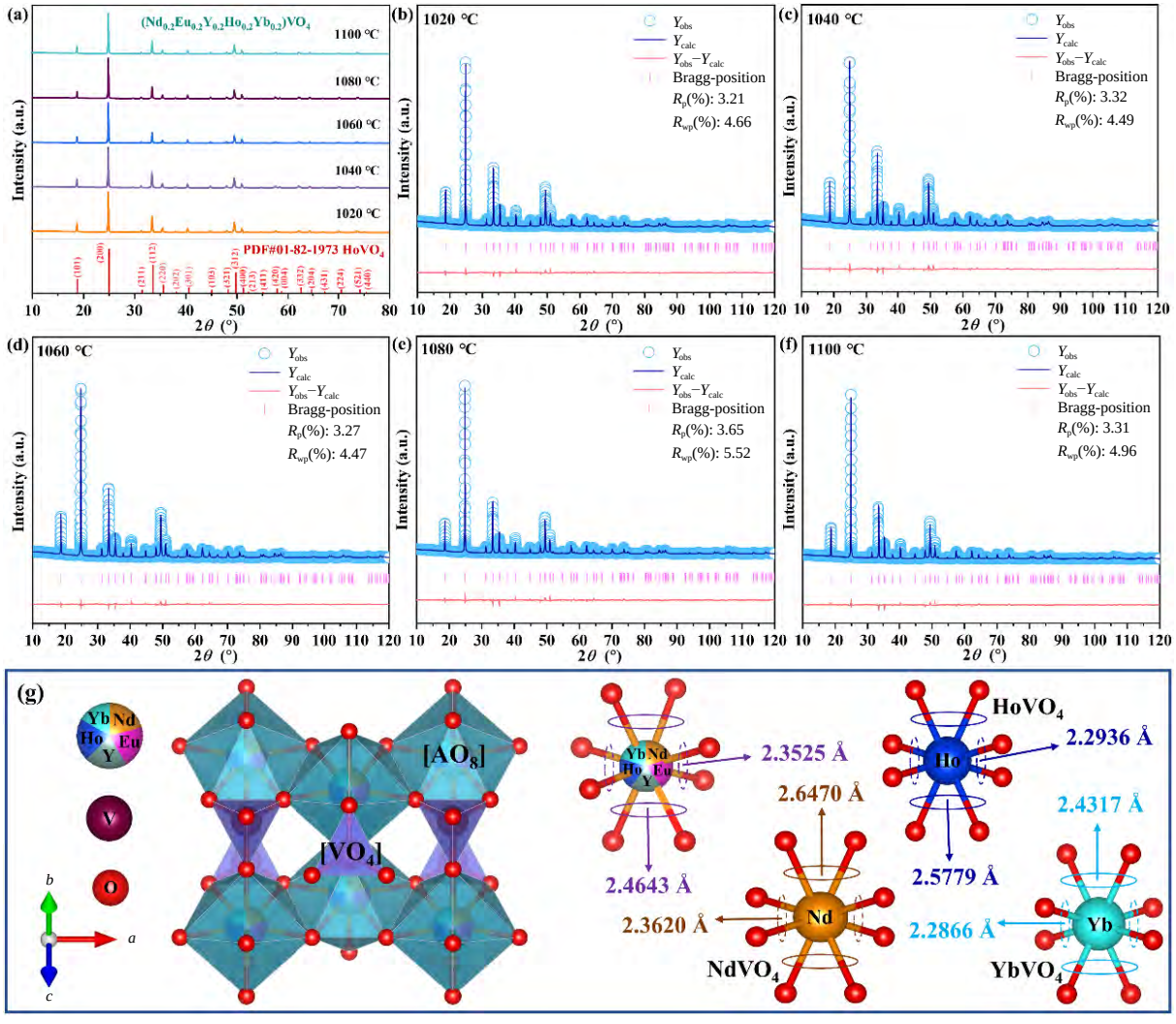

Fig. 2 (a) XRD patterns of $(Nd_{0.2}Eu_{0.2}Y_{0.2}Ho_{0.2}Yb_{0.2})VO_4$ ceramics sintered at different sintering temperatures, (b–f) refinement patterns of $(Nd_{0.2}Eu_{0.2}Y_{0.2}Ho_{0.2}Yb_{0.2})VO_4$ ceramics, and (g) crystal structure of $(Nd_{0.2}Eu_{0.2}Y_{0.2}Ho_{0.2}Yb_{0.2})VO_4$ ceramics and disparity of bond lengths in dodecahedral ceramics compared with those of traditional zircon ceramics.

Table 1 Details of crystallographic data and structural refinement conditions for all $(Nd_{0.2}Eu_{0.2}Y_{0.2}Ho_{0.2}Yb_{0.2})VO_4$ ceramics

Sintering temperature	1020 °C	1040 °C	1060 °C	1080 °C	1100 °C
Radiation type	Cu $K\alpha_1$	Cu $K\alpha_1$	Cu $K\alpha_1$	Cu $K\alpha_1$	Cu $K\alpha_1$
The range of 2θ	5°–120°	5°–120°	5°–120°	5°–120°	5°–120°
No. of data points	8837	8837	8837	8837	8837
T (K)	298	298	298	298	298
Reduced χ^2	1.09	1.14	1.01	1.37	1.25
R_{wp} (%)	4.66	4.49	4.47	5.52	4.96
R_p (%)	3.21	3.32	3.27	3.65	3.31
Crystal system	Tetragonal ($I4_1/amd$)	Tetragonal ($I4_1/amd$)	Tetragonal ($I4_1/amd$)	Tetragonal ($I4_1/amd$)	Tetragonal ($I4_1/amd$)
$a = b$ (Å)	7.17008	7.16996	7.16935	7.17016	7.17045
c (Å)	6.32566	6.32562	6.32561	6.32566	6.32598
V (Å^3)	325.199	325.189	325.134	325.209	325.253

4.47%–5.52% and profile factor (R_p) = 3.21%–3.65%, were low for all $(Nd_{0.2}Eu_{0.2}Y_{0.2}Ho_{0.2}Yb_{0.2})VO_4$ high-entropy ceramics, thereby demonstrating the reliability of the refinement outcomes.

A schematic diagram of the crystal structure of $(Nd_{0.2}Eu_{0.2}Y_{0.2}Ho_{0.2}Yb_{0.2})VO_4$ is shown in Fig. 2(g). The phase stability of $REVO_4$ is contingent upon the ionic radius of the RE^{3+} ions, with the majority of rare earth elements (RE = Pr–Lu, Sc, and Y) exhibiting a zircon-type crystallographic structure [26]. The $[VO_4]$ tetrahedra, characterized by their equidistant V-O bond lengths, and the $[REO_8]$ dodecahedra alternately share edges along the crystallographic c-axis, constituting a zircon-type structure. In the $(Nd_{0.2}Eu_{0.2}Y_{0.2}Ho_{0.2}Yb_{0.2})VO_4$ high-entropy ceramics, the disparity in bond lengths (2.4643 and 2.3525 Å) within the dodecahedral coordination is less pronounced than

that in traditional zircon ceramics (Fig. 2(g)), as exemplified by the more significant difference observed in $NdVO_4$ (2.6470 and 2.3620 Å) [16], $HoVO_4$ (2.5779 and 2.2936 Å) [17], and $YbVO_4$ (2.4317 and 2.2866 Å) [17]. This suggests that the structural stability of the high-entropy ceramics is comparatively enhanced.

To elucidate the alterations in the crystal structure attributable to the high-entropy effect, room-temperature Raman spectroscopy was employed to analyze all $(Nd_{0.2}Eu_{0.2}Y_{0.2}Ho_{0.2}Yb_{0.2})VO_4$ ceramic samples. Group theory calculations predict the presence of 12 Raman modes, specifically $2A_{1g}$, $4B_{1g}$, $1B_{2g}$, and $5E_g$, for the tetragonal zircon structure, which belongs to space group $I4_1/amd$. The absence of certain Raman modes in Fig. 3(a) is likely attributed to the low Raman scattering cross sections of these modes, as well as the spectral overlap between numerous A_g and B_g modes. The Raman spectroscopic data corroborate the zircon-type structure of the synthesized $(Nd_{0.2}Eu_{0.2}Y_{0.2}Ho_{0.2}Yb_{0.2})VO_4$ ceramics, which aligns with previously reported findings [27] and the XRD analysis depicted in Fig. 2(a). The Raman modes at 828 and 806 cm^{-1} for $(Nd_{0.2}Eu_{0.2}Y_{0.2}Ho_{0.2}Yb_{0.2})VO_4$ are attributed to asymmetric V–O stretching vibrations, with symmetric and asymmetric bending modes at approximately 379 and 484 cm^{-1}, respectively [28]. Raman peaks appear near 886 cm^{-1}, belonging to the symmetric V–O bond stretching mode (A_{1g}) of the zircon phase. Fewer vibrational peaks were observed for RE–O bonds, possibly because of the lower coordination number (8) and the high symmetry (D_{2d}) of the RE^{3+} ions [29]. The amplitude of the lattice and nonharmonic vibrational modes diminishes with a reduction in the full width at half maximum (FWHM), consequently resulting in a reduction in the intrinsic dielectric loss and an increase in the $Q \times f$ [28,30]. As shown in Fig. 3(b) and Table 2, $(Nd_{0.2}Eu_{0.2}Y_{0.2}Ho_{0.2}Yb_{0.2})VO_4$ high-entropy ceramics have narrower Raman FWHM values than $HoVO_4$ does.

HRTEM was also employed to characterize the $(Nd_{0.2}Eu_{0.2}Y_{0.2}Ho_{0.2}Yb_{0.2})VO_4$ and $HoVO_4$ ceramics. The SAED pattern of the $(Nd_{0.2}Eu_{0.2}Y_{0.2}Ho_{0.2}Yb_{0.2})VO_4$ ceramics (Fig. 4(a)) was identified as tetragonal zircon along the [010] zone axis. The HRTEM image of the $(Nd_{0.2}Eu_{0.2}Y_{0.2}Ho_{0.2}Yb_{0.2})VO_4$ ceramics, as depicted in Fig. 4(b), reveals distinct lattice fringes with interplanar spacings of 0.476 and 0.362 nm, corresponding to the (101) and (200) facets, respectively. These values are marginally larger than the values of 0.471 nm for the (101) and 0.356 nm for the (200) facets reported in the powder diffraction file (PDF#01-82-1973), which is attributed to differences in the ionic radii of the A-site. Notably, the HRTEM images (Figs. 4(d) and 4(f)) and the atomic inverse fast Fourier transform (IFFT)-filtered images (Figs. 4(e) and 4(g)) of the $HoVO_4$ ceramics compared with the $(Nd_{0.2}Eu_{0.2}Y_{0.2}Ho_{0.2}Yb_{0.2})VO_4$ high-entropy ceramics (Fig. 4(b)) reveal the presence of many point defects and lattice dislocations within the structure. It is widely accepted that the high-entropy effect induces an increase in configurational entropy and a concomitant reduction in Gibbs free energy, which significantly affects the microstructure and stability of a material, culminating in an increased incidence of lattice defects and distortions [31]. However, the formation of a high-entropy effect at the A-site in $(Nd_{0.2}Eu_{0.2}Y_{0.2}Ho_{0.2}Yb_{0.2})VO_4$ rectifies the inherent lattice distortions and defects in conventional zircon ceramics, potentially enhancing structural stability and diminishing dielectric losses. The TEM-energy-dispersive X-ray spectroscopy (EDS) mapping of $(Nd_{0.2}Eu_{0.2}Y_{0.2}Ho_{0.2}Yb_{0.2})VO_4$, as illustrated in Fig. 4(h), reveals highly uniform elemental distributions at the nanoscale. Consequently, this further confirms our judgment on the single-phase $(Nd_{0.2}Eu_{0.2}Y_{0.2}Ho_{0.2}Yb_{0.2})VO_4$ high-entropy ceramics.

SEM images of the $(Nd_{0.2}Eu_{0.2}Y_{0.2}Ho_{0.2}Yb_{0.2})VO_4$ high-entropy ceramics sintered at various temperatures are presented in Figs. 5(a)–5(e). As the sintering temperature increased, the porosity within the sintered samples decreased, and the average

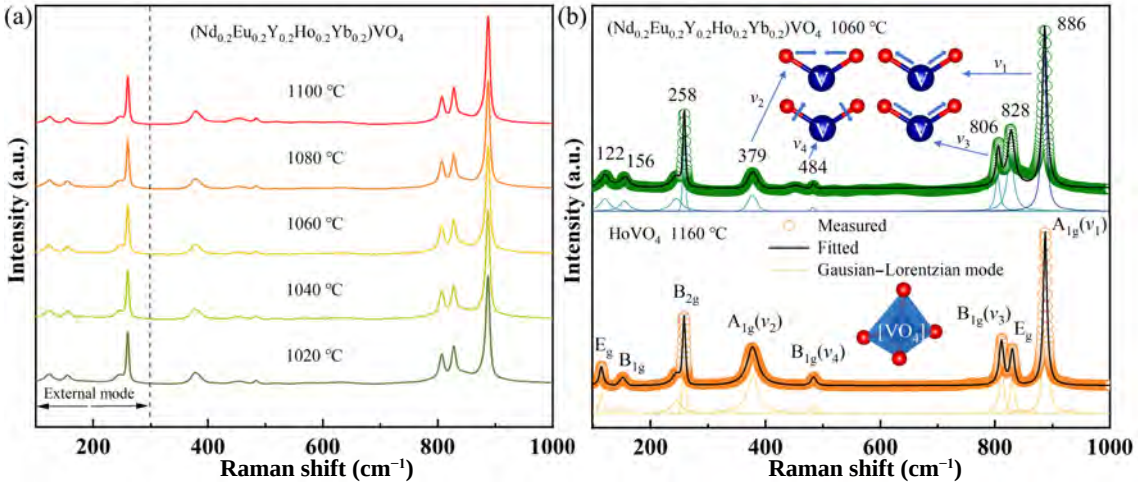

Fig. 3 (a) Raman spectra of $(Nd_{0.2}Eu_{0.2}Y_{0.2}Ho_{0.2}Yb_{0.2})VO_4$. (b) Gaussian function fitting for $(Nd_{0.2}Eu_{0.2}Y_{0.2}Ho_{0.2}Yb_{0.2})VO_4$ and $HoVO_4$ ceramics. Illustrations represent Raman modes, vibrations, and structure schematic diagrams (ν_1, ν_2, ν_3, and ν_4 represent symmetric stretch, symmetric bending, antisymmetric stretch, and antisymmetric bending, respectively).

Table 2 Wavenumbers and Raman FWHMs of $(Nd_{0.2}Eu_{0.2}Y_{0.2}Ho_{0.2}Yb_{0.2})VO_4$ and $HoVO_4$ ceramics

Ceramic	Vibrational mode	B_{2g}	A_{1g} (ν_2)	B_{1g} (ν_4)	B_{1g} (ν_3)	E_g	A_{1g} (ν_1)
$(Nd_{0.2}Eu_{0.2}Y_{0.2}Ho_{0.2}Yb_{0.2})VO_4$	Wavenumber (cm^{-1})	258	379	484	806	828	886
	FWHM (cm^{-1})	5.07	18.98	6.80	9.15	13.9	7.35
$HoVO_4$	Wavenumber (cm^{-1})	259	380	487	814	831	889
	FWHM (cm^{-1})	5.68	23.36	10.55	9.75	8.68	7.61

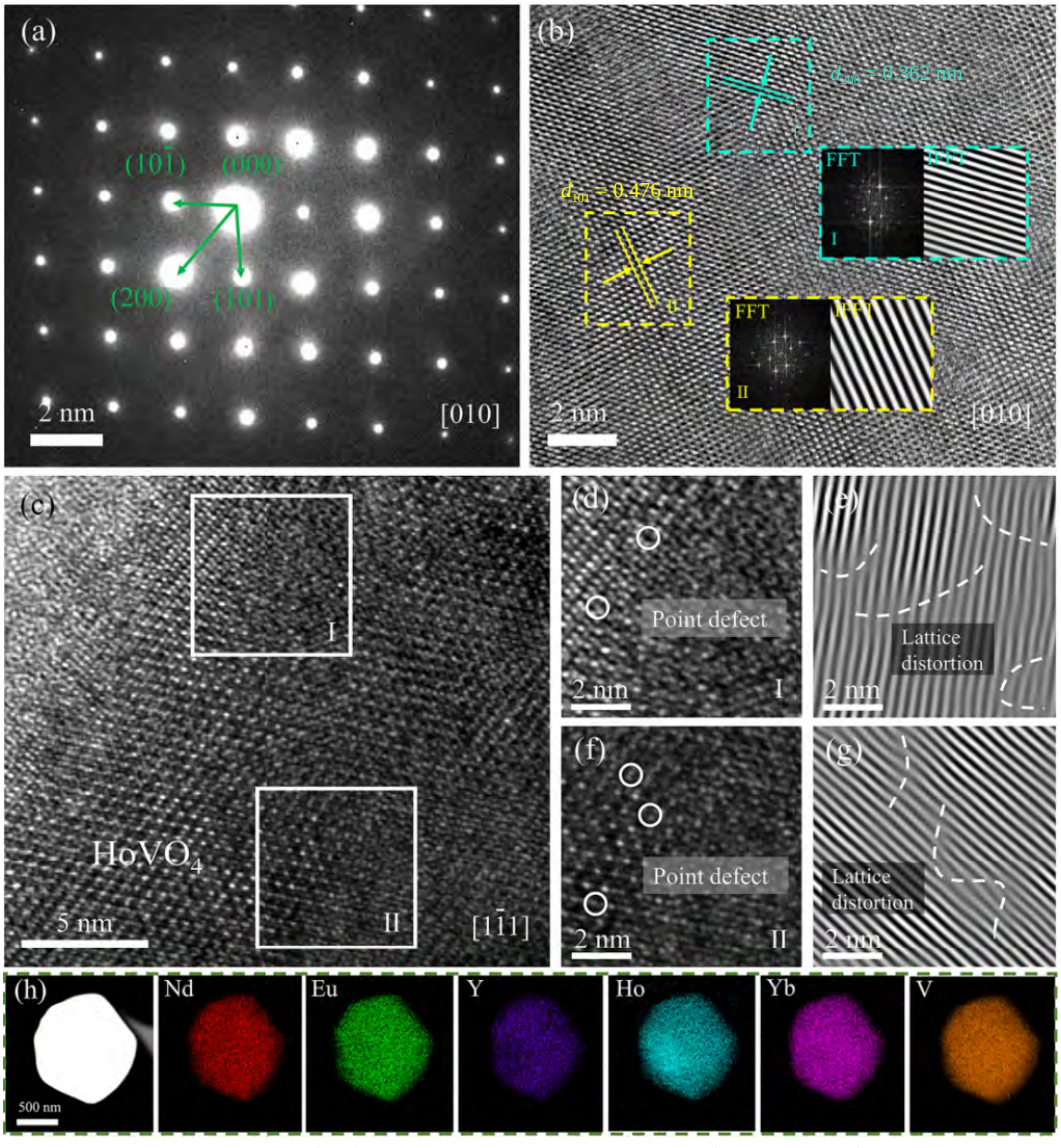

Fig. 4 (a, b) SAED patterns and HRTEM images of $(Nd_{0.2}Eu_{0.2}Y_{0.2}Ho_{0.2}Yb_{0.2})VO_4$. Inset images are fast Fourier transform (FFT) map, IFFT map, and lattice spacing. (c, d, f) HRTEM images and (e, g) corresponding IFFT patterns of $HoVO_4$. (h) TEM-EDS mappings of $(Nd_{0.2}Eu_{0.2}Y_{0.2}Ho_{0.2}Yb_{0.2})VO_4$ (different color points represent uniformly distributed Nd, Eu, Y, Ho, Yb, and V).

grain size increased from 3.11 to 4.69 μm. The variation in both the bulk and relative densities of $(Nd_{0.2}Eu_{0.2}Y_{0.2}Ho_{0.2}Yb_{0.2})VO_4$ high-entropy ceramics with respect to the sintering temperature is illustrated in Fig. 5(f). The compactness of the samples peaks at 1060 °C, after which it decreases with increasing temperature. This decrease in density is attributed to abnormal grain growth. Within the examined sintering temperature range, the relative density of $(Nd_{0.2}Eu_{0.2}Y_{0.2}Ho_{0.2}Yb_{0.2})VO_4$ ceramics exceeded 96% (reaching a maximum value of 97.1% at 1060 °C), indicating excellent compactness that aligns with the SEM observations. Additionally, EDS mapping was conducted to determine whether the elemental ratios in the $(Nd_{0.2}Eu_{0.2}Y_{0.2}Ho_{0.2}Yb_{0.2})VO_4$ ceramics adhered to the intended compositions. Figure 5(g) shows the elemental distribution, with specific proportions indicated within the figure. The elements Nd, Eu, Y, Ho, Yb, V, and O were found to be uniformly dispersed, with percentages closely matching the targeted ratios, thereby verifying the successful preparation of $(Nd_{0.2}Eu_{0.2}Y_{0.2}Ho_{0.2}Yb_{0.2})VO_4$ high-entropy ceramics.

Figure 6(a) shows the temperature-dependent variation in the measured ε_r of the $(Nd_{0.2}Eu_{0.2}Y_{0.2}Ho_{0.2}Yb_{0.2})VO_4$ high-entropy ceramics, which initially increases and then decreases (11.21→11.55→11.49), peaking at 1060 °C (11.55), mirroring the trend observed in the relative density of the sintered samples. At microwave frequencies, dielectric materials predominantly exhibit ionic displacement polarization and electronic displacement polarization [32]. Owing to the higher sensitivity of electrons to electric fields, electronic polarization contributes less to the relative permittivity, rendering ionic displacement polarization more significant. The Clausius-Mossotti equation elucidates the correlation between ε_r and microscopic ionic polarizability [33,34]. By applying Shannon's additive rule for polarizability, the theoretical permittivity ($\varepsilon_{r(C-M)}$) of the dielectric ceramics can be approximated, as delineated in Eqs. (2) and (3):

$$\varepsilon_{r(C-M)} = \frac{3V_m + 8\pi\alpha_m}{3V_m - 4\pi\alpha_m} \tag{2}$$

$$\alpha_m = 0.2\alpha_{Nd}^{3+} + 0.2\alpha_{Eu}^{3+} + 0.2\alpha_{Y}^{3+} + 0.2\alpha_{Ho}^{3+} + 0.2\alpha_{Yb}^{3+} + \alpha_{V}^{5+} + 4\alpha_{O}^{2-} \tag{3}$$

where V_m refers to the molar volume, and α_m denotes the

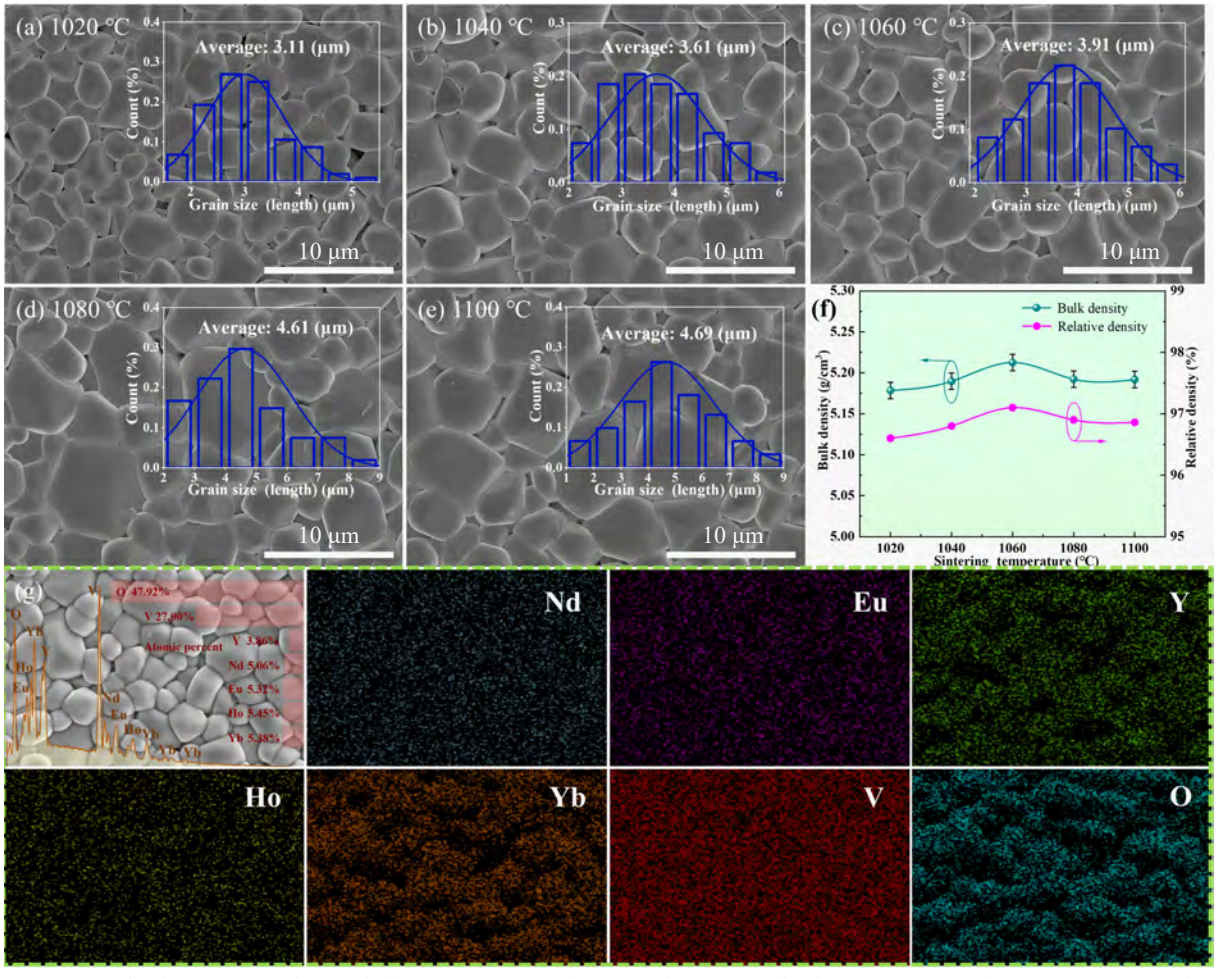

Fig. 5 SEM images of $(Nd_{0.2}Eu_{0.2}Y_{0.2}Ho_{0.2}Yb_{0.2})VO_4$ high-entropy ceramics and corresponding grain size distributions: (a) 1020 °C, (b) 1040 °C, (c) 1060 °C, (d) 1080 °C, and (e) 1100 °C. (f) Bulk and relative densities of high-entropy ceramics sintered at various temperatures. (g) EDS mappings and element proportions of $(Nd_{0.2}Eu_{0.2}Y_{0.2}Ho_{0.2}Yb_{0.2})VO_4$ ceramics (different color points represent uniformly distributed Nd, Eu, Y, Ho, Yb, V, and O).

molecular polarizability. The ionic polarizabilities of Nd^{3+} (α_{Nd}^{3+}), Eu^{3+} (α_{Eu}^{3+}), Y^{3+} (α_{Y}^{3+}), Ho^{3+} (α_{Ho}^{3+}), Yb^{3+} (α_{Yb}^{3+}), V^{5+} (α_{V}^{5+}), and O^{2-} (αO^{2-}) are 5.01, 4.53, 3.81, 3.97, 3.58, 2.92, and 2.01 Å^3, respectively. The calculated $\varepsilon_{r(C-M)}$ is approximately 11.65, which slightly exceeds the experimentally determined value (ε_r). The relative discrepancy between these values is −0.8%, suggesting that the strain within the high-entropy ceramic structure is minimal. This is consistent with the general consensus that deviations exceeding 5% from the expected value may indicate anomalous physical properties and structural characteristics [35].

Figure 6(b) shows the temperature coefficient of the resonance frequency (τ_f) of the $(Nd_{0.2}Eu_{0.2}Y_{0.2}Ho_{0.2}Yb_{0.2})VO_4$ high-entropy ceramics at different sintering temperatures. The τ_f of $(Nd_{0.2}Eu_{0.2}Y_{0.2}Ho_{0.2}Yb_{0.2})VO_4$ initially decreased but then increased, which was inversely related to the trend observed for ε_r. At the optimal densification temperature of 1060 °C, the τ_f of the high-entropy ceramics is −37.3 ppm/°C. The τ_f of microwave dielectric ceramics, as delineated by Eq. (4), is composed of two distinct components: the temperature coefficient of the permittivity (τ_ε) and the coefficient of thermal expansion (α_L) of the ceramic material [36,37].

$$\tau_f = -\left(\alpha_L + \frac{1}{2}\tau_\varepsilon\right) \quad (4)$$

The a_L values of $(Nd_{0.2}Eu_{0.2}Y_{0.2}Ho_{0.2}Yb_{0.2})VO_4$ high-entropy ceramics and $HoVO_4$ ceramics were determined within the temperature range from 30 to 500 °C, and the results are presented in Fig. 6(c). The α_L values of $(Nd_{0.2}Eu_{0.2}Y_{0.2}Ho_{0.2}Yb_{0.2})VO_4$ and $HoVO_4$ are 7.9 and 7.1 ppm/°C, respectively. Given their proximity, the disparity in τ_f primarily hinges on τ_ε. The calculated values of τ_ε for $(Nd_{0.2}Eu_{0.2}Y_{0.2}Ho_{0.2}Yb_{0.2})VO_4$ and $HoVO_4$ ceramics are 55.2 and 20.8 ppm/°C, respectively. Figure 6(d) shows the τ_f values of vanadium-based zircon ceramics as a function of the cationic radius of the A-site dodecahedron. As the rare-earth ion radius increases, the τ_f of the system fluctuates but generally decreases. Compared with that of traditional zircon ceramics, the τ_f value of $(Nd_{0.2}Eu_{0.2}Y_{0.2}Ho_{0.2}Yb_{0.2})VO_4$ high-entropy ceramics is in good agreement with the fitting curve, indicating that the crystal structure of the high-entropy ceramics is stable and is least affected by other mechanisms. The negative τ_f value of the $(Nd_{0.2}Eu_{0.2}Y_{0.2}Ho_{0.2}Yb_{0.2})VO_4$ high-entropy ceramics still exceeds the practical requirements. Therefore, we prepared $(1-x)(Nd_{0.2}Eu_{0.2}Y_{0.2}Ho_{0.2}Yb_{0.2})VO_4$–$xTiO_2$ composite ceramics via the standard solid-state reaction method (inset of Fig. 6(b)). A near-zero τ_f of −2.4 ppm/°C was obtained for the $0.925(Nd_{0.2}Eu_{0.2}Y_{0.2}Ho_{0.2}Yb_{0.2})VO_4$–$0.075TiO_2$ composite ceramics (Fig. 6(d)). However, the introduction of the second phase of TiO_2 results in a significant reduction in the $Q \times f$ value (37,500 GHz).

Figure 7 presents the temperature-dependent variations in the dielectric properties (ε_r and dielectric loss tanδ) of the $(Nd_{0.2}Eu_{0.2}Y_{0.2}Ho_{0.2}Yb_{0.2})VO_4$ and $HoVO_4$ ceramics across the range of 30–300 °C at frequencies from 5 kHz to 1 MHz. The

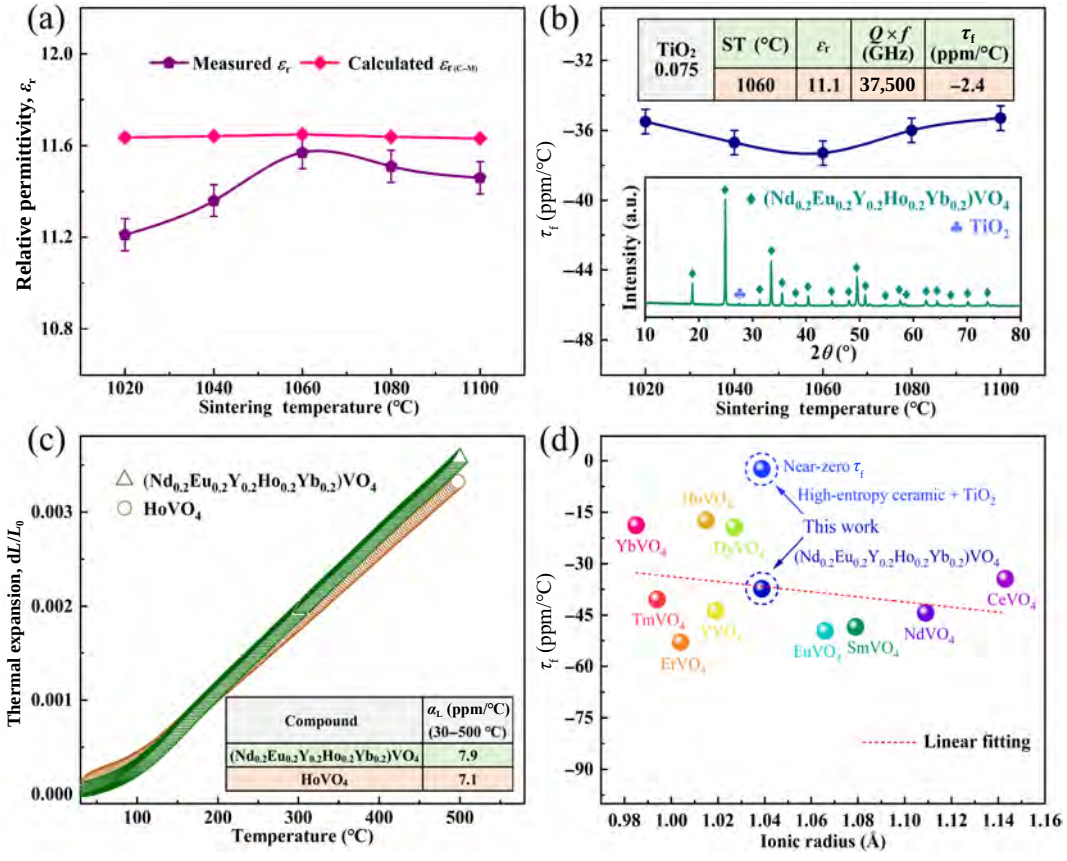

Fig. 6 Variations in (a) measured permittivity (ε_r) and calculated permittivity ($\varepsilon_{r(C-M)}$) and (b) τ_f of $(Nd_{0.2}Eu_{0.2}Y_{0.2}Ho_{0.2}Yb_{0.2})VO_4$ high-entropy ceramics with different sintering temperatures. The inset shows XRD pattern and microwave dielectric properties of $0.925(Nd_{0.2}Eu_{0.2}Y_{0.2}Ho_{0.2}Yb_{0.2})VO_4$–$0.075TiO_2$ ceramics sintered at 1060 °C. (c) Thermal expansion data of $(Nd_{0.2}Eu_{0.2}Y_{0.2}Ho_{0.2}Yb_{0.2})VO_4$ and $HoVO_4$ ceramics. (d) τ_f values of vanadium-based zircon ceramics as a function of rare-earth ion radius.

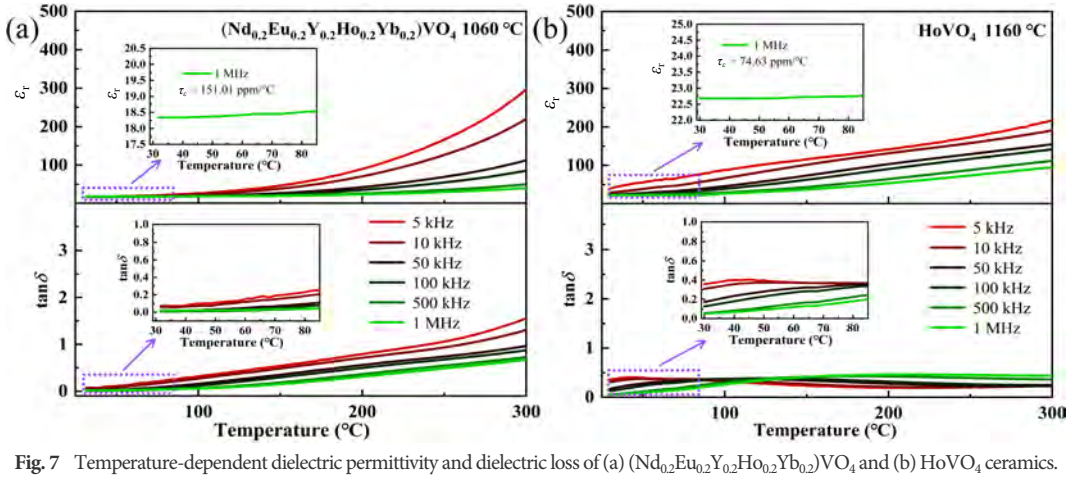

Fig. 7 Temperature-dependent dielectric permittivity and dielectric loss of (a) $(Nd_{0.2}Eu_{0.2}Y_{0.2}Ho_{0.2}Yb_{0.2})VO_4$ and (b) $HoVO_4$ ceramics.

experimentally determined τ_ε values (151.01 and 74.63 ppm/°C) align with the projected trend, yet they exceed the calculated values. This discrepancy could stem from variations in the test temperature, the instrumentation employed, and the frequency of measurement. The dielectric loss curve of the $HoVO_4$ ceramics reveals a broad peak in dielectric loss across the specified temperature range, which shifts toward higher temperatures with increasing frequency. This finding suggests that the charge carriers within the ceramics undergo a thermal activation process, potentially attributable to the formation of oxygen vacancies or other lattice defects within the crystal structure. The dielectric loss of $(Nd_{0.2}Eu_{0.2}Y_{0.2}Ho_{0.2}Yb_{0.2})VO_4$ high-entropy ceramics results in enhanced temperature stability at lower temperatures, potentially attributable to the amelioration of lattice distortions.

Figure 8(a) depicts the quality factor ($Q \times f$) for the $(Nd_{0.2}Eu_{0.2}Y_{0.2}Ho_{0.2}Yb_{0.2})VO_4$ high-entropy ceramics across a range of sintering temperatures. The $Q \times f$ of $(Nd_{0.2}Eu_{0.2}Y_{0.2}Ho_{0.2}Yb_{0.2})VO_4$ tends to increase initially and then decreases as the sintering temperature increases. This trend is likely due to changes in the porosity, grain boundary characteristics, and grain size distribution within the samples in response to temperature variations. At an optimal densification temperature of 1060 °C, $(Nd_{0.2}Eu_{0.2}Y_{0.2}Ho_{0.2}Yb_{0.2})VO_4$ high-entropy ceramics achieve the highest $Q \times f$ value of 76,400 GHz

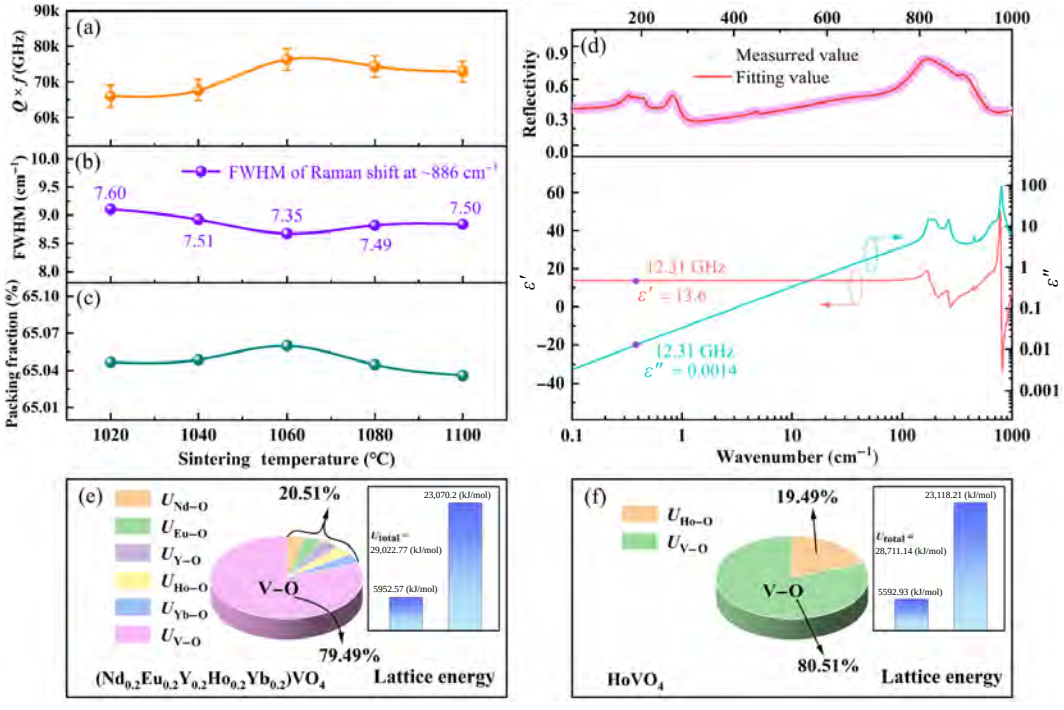

Fig. 8 (a) $Q \times f$ value, (b) Raman FWHM, and (c) packing fraction of $(Nd_{0.2}Eu_{0.2}Y_{0.2}Ho_{0.2}Yb_{0.2})VO_4$ high-entropy ceramics sintered at different temperatures. (d) Measured and fitted infrared reflectivity spectra, real parts, and imaginary parts of complex permittivity for high-entropy ceramics. U of (e) $(Nd_{0.2}Eu_{0.2}Y_{0.2}Ho_{0.2}Yb_{0.2})VO_4$ and (f) $HoVO_4$ ceramics.

(at 12.31 GHz), which is more than twofold greater than that of conventional zircon ceramics. Studies have demonstrated that a reduction in the Raman FWHM correlates with a decrease in the amplitude of the lattice and anharmonic vibrational modes, consequently leading to a reduction in intrinsic dielectric loss and an increase in $Q \times f$ [38]. Figure 8(b) shows that the $Q \times f$ of $(Nd_{0.2}Eu_{0.2}Y_{0.2}Ho_{0.2}Yb_{0.2})VO_4$ high-entropy ceramics is inversely related to the trend observed for the FWHM. At 1060 °C, the maximum $Q \times f$ value coincided with the minimum FWHM, a finding that is consistent with Ref. [39]. The packing fraction can be used to analyze the relationship between the crystal structure and the intrinsic $Q \times f$ value. As shown in Fig. 8(c), the changing trend of the packing fraction is highly consistent with the $Q \times f$ value. An increased packing fraction reduces the lattice vibration space, leading to a decrease in the dielectric loss, which corresponds to a higher $Q \times f$ value [40].

To delve deeper into the intrinsic dielectric loss characteristics of the $(Nd_{0.2}Eu_{0.2}Y_{0.2}Ho_{0.2}Yb_{0.2})VO_4$ high-entropy ceramics, an analysis of the infrared reflectance spectrum was conducted employing the classical harmonic oscillator model [41]:

$$\varepsilon^*(\omega) = \varepsilon_\infty + \sum_{j=1}^{n} \frac{\omega_{pj}^2}{\omega_{oj}^2 - \omega^2 - j\gamma_j\omega} \tag{5}$$

where $\varepsilon^*(\omega)$ represents the complex dielectric function, ε_∞ denotes the high-frequency dielectric constant attributable to electronic polarization, and γ_j, ω_{oj}, and ω_{pj} correspond to the damping factor, the oscillation frequency, and the plasma frequency of the j-th Lorentz oscillator, respectively. The complex reflectivity, $R(\omega)$, is expressed as Eq. (6) [42]:

$$R(\omega) = \left| \frac{1 - \sqrt{\varepsilon^*(\omega)}}{1 + \sqrt{\varepsilon^*(\omega)}} \right|^2 \tag{6}$$

Within the microwave frequency range where $\omega << \omega_{oj}$, the real and imaginary components of the complex permittivity, as well as tanδ, are articulated as Eqs. (7)–(9) [43]:

$$\varepsilon'(\omega) = \varepsilon_\infty + \sum_{j=1}^{n} \varepsilon_j = \varepsilon_\infty + \sum_{j=1}^{n} \frac{\omega_{pj}^2}{\omega_{oj}^2} \tag{7}$$

$$\varepsilon''(\omega) = \sum_{j=1}^{n} \frac{\omega_{oj}^2 \omega \gamma_j}{\omega_{oj}^2} \tag{8}$$

$$\tan\delta = \frac{\varepsilon''}{\varepsilon'} = \omega \sum_{j=1}^{n} \frac{\Delta\varepsilon_j \gamma_j}{\omega_{oj}^2 (\varepsilon_\infty + \sum_{j=1}^{n} \Delta\varepsilon_j)} \tag{9}$$

The fitted infrared reflectivity values and complex permittivity for the high-entropy ceramics $(Nd_{0.2}Eu_{0.2}Y_{0.2}Ho_{0.2}Yb_{0.2})VO_4$ are shown in Fig. 8(d), and the parameters are listed in Table 3. The real part of the complex permittivity (ε' = 13.6) of $(Nd_{0.2}Eu_{0.2}Y_{0.2}Ho_{0.2}Yb_{0.2})VO_4$ closely approximates the measured ε_r of 11.55 and the calculated $\varepsilon_{r(C-M)}$ (11.65) from the Clausius-Mossotti Equation. The calculated dielectric loss for $(Nd_{0.2}Eu_{0.2}Y_{0.2}Ho_{0.2}Yb_{0.2})VO_4$ was found to be 1.42×10^{-4} at a frequency of 12.31 GHz, which is marginally lower than that obtained via the TE_{011} method. The extrapolated intrinsic $Q \times f$ for the microwave frequency band is estimated at 117,500 GHz, slightly surpassing the experimental value of 76,400 GHz. The $Q \times f$ value of $(Nd_{0.2}Eu_{0.2}Y_{0.2}Ho_{0.2}Yb_{0.2})VO_4$ high-entropy ceramics can be further enhanced through structural regulation and optimization of the processing parameters.

The lattice energy (U) for each chemical bond within the high-entropy ceramics $(Nd_{0.2}Eu_{0.2}Y_{0.2}Ho_{0.2}Yb_{0.2})VO_4$ was determined via P–V–L chemical bond theory, offering insights into the correlation between the crystal structure and dielectric loss. Lattice energy is intricately linked to $Q \times f$ and is a critical metric for assessing the binding strength of chemical bonds [44,45].

The equations utilized for the calculations are presented as Eqs. (10)–(13):

$$U_b^\mu = U_{bi}^\mu + U_{bc}^\mu \tag{10}$$

$$U_{bi}^\mu = 1270\frac{(m+n)\,Z_+^\mu Z_-^\mu}{d^\mu}\left(1-\frac{0.4}{d^\mu}\right)f_i^\mu \tag{11}$$

$$U_{bc}^\mu = 2100m\frac{(Z_+^\mu)^{1.64}}{(d^\mu)^{0.75}}f_c^\mu \tag{12}$$

$$U_{\text{total}} = \sum\nolimits_\mu U_b^\mu \tag{13}$$

where U_{bc}^μ and U_{bi}^μ represent the lattice energies corresponding to the ionic and covalent contributions, respectively, and Z_+^μ and Z_-^μ represent the chemical bonding valences associated with cations and anions within the chemical bond μ, respectively. The bond length is denoted as d^μ, and the m and n values are obtained from the binary bond formula. The lattice energy indicates the binding force between anions and cations, as evidenced by nonharmonic vibrations, and can be utilized to predict intrinsic losses. Typically, increased total lattice energy (U_{total}) of a compound is associated with reduced intrinsic losses, thereby resulting in a higher product of $Q \times f$ [46,47]. The data reveal that U_{total} for $(Nd_{0.2}Eu_{0.2}Y_{0.2}Ho_{0.2}Yb_{0.2})VO_4$ high-entropy ceramics, at 29,022.77 kJ/mol, substantially exceeds that of $HoVO_4$, which is 28,711.14 kJ/mol. In the $(Nd_{0.2}Eu_{0.2}Y_{0.2}Ho_{0.2}Yb_{0.2})VO_4$ and $HoVO_4$ ceramics, the U of V–O bond constitutes approximately 80%, as illustrated in Figs. 8(e) and 8(f), a value notably higher than that of the A–O bond, underscoring the stability of the tetrahedral configuration. More significantly, the average lattice energy at the A-site within the $(Nd_{0.2}Eu_{0.2}Y_{0.2}Ho_{0.2}Yb_{0.2})VO_4$ high-entropy ceramics exceeds that observed in conventional zircon ceramics, suggesting that the high-entropy effect strengthens the bonding forces and bolsters the structural integrity of the dodecahedral unit. Consequently, the reduction in the bond strain, increase in the lattice energy, and increase in the structural stability of $(Nd_{0.2}Eu_{0.2}Y_{0.2}Ho_{0.2}Yb_{0.2})VO_4$ high-entropy ceramics following the repair of lattice distortion are among the key factors contributing to its superior $Q \times f$ value compared with that of conventional zircon ceramics.

Table 3 Phonon parameters obtained from fitting of infrared reflectivity spectra of $(Nd_{0.2}Eu_{0.2}Y_{0.2}Ho_{0.2}Yb_{0.2})VO_4$

$(Nd_{0.2}Eu_{0.2}Y_{0.2}Ho_{0.2}Yb_{0.2})VO_4$				
Mode	ω_{oj}	ω_{pj}	γ_j	$\triangle\varepsilon_j$
1	118.06	175.720	109.880	2.22
2	143.22	89.730	34.970	0.39
3	174.57	44.710	3.710	0.06
4	197.29	273.970	37.570	1.93
5	237.22	121.830	30.348	0.26
6	264.49	242.200	22.200	0.83
7	449.90	79.065	7.870	0.03
8	650.32	593.800	89.840	0.83
9	798.68	1524.400	35.513	3.64
10	857.11	465.690	50.856	0.29
11	888.01	288.760	24.737	0.10
$\varepsilon_\infty = 2.35$; $\varepsilon_0 = 13.6$				

For ceramic materials, defects induced by the sintering process also represent a significant source of dielectric loss. Figure 9 depicts the Arrhenius relationship between the conductivity of the $(Nd_{0.2}Eu_{0.2}Y_{0.2}Ho_{0.2}Yb_{0.2})VO_4$ and $HoVO_4$ ceramics ($\sigma = 1/\rho_{dc}$) and the temperature, as well as the conductive activation energy (E_a), which can be affected by lattice defects and is derived from Eq. (14) [48,49]:

$$\sigma = \sigma_0\exp(-E_a/kT) \tag{14}$$

where σ_0 represents the index prefactor, k denotes the Boltzmann constant, and T represents the thermodynamic temperature. E_a represents the migration activation energy of charge carriers, which is influenced by the concentration of oxygen vacancies and free carriers. Typically, the activation energy associated with double-ionized oxygen vacancies in ceramics within the high-temperature domain is estimated to be within the range of 0.6–1.2 eV [50]. The inset in Fig. 9 shows the variation in the direct current resistivity (ρ_{dc}) of the $(Nd_{0.2}Eu_{0.2}Y_{0.2}Ho_{0.2}Yb_{0.2})VO_4$ and $HoVO_4$ ceramics as a function of temperature. The calculations reveal that the direct current resistivity of the $(Nd_{0.2}Eu_{0.2}Y_{0.2}Ho_{0.2}Yb_{0.2})VO_4$ ceramics is 5.67×10^7 Ω·cm, which exceeds that of the $HoVO_4$ ceramics, with a resistivity of 4.63×10^7 Ω·cm. Analysis reveals that E_a for the $(Nd_{0.2}Eu_{0.2}Y_{0.2}Ho_{0.2}Yb_{0.2})VO_4$ ceramics optimized at the sintering temperature is 1.16 eV, whereas it is 1.02 eV for the $HoVO_4$ ceramics. Higher activation energies are commonly associated with lower defect densities [51,52], which also confirms the TEM analysis results.

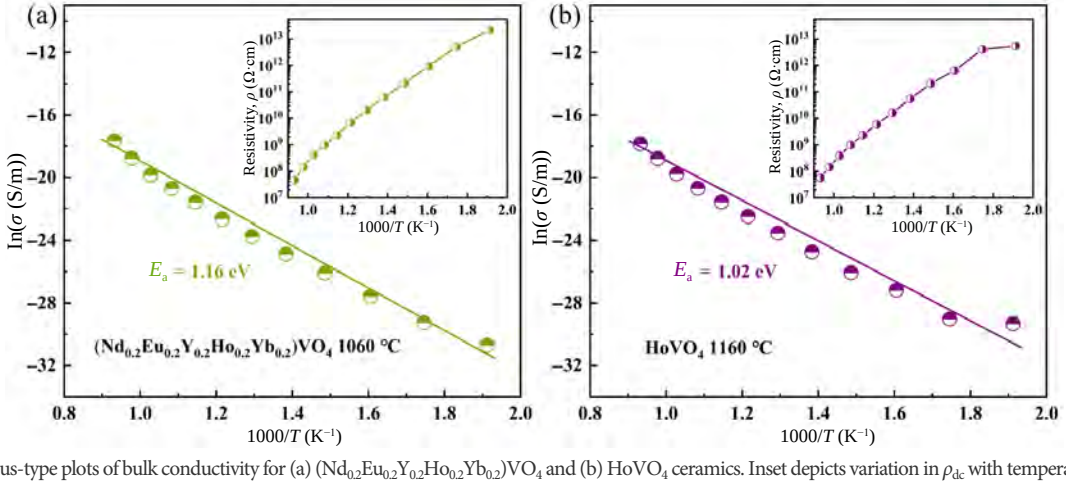

Fig. 9 Arrhenius-type plots of bulk conductivity for (a) $(Nd_{0.2}Eu_{0.2}Y_{0.2}Ho_{0.2}Yb_{0.2})VO_4$ and (b) $HoVO_4$ ceramics. Inset depicts variation in ρ_{dc} with temperature increasing.

4 Conclusions

In summary, a high-entropy strategy has been introduced to repair A-site dodecahedral distortion in zircon ceramics. This strategy involves enhancing bonding, reducing lattice defects, and enhancing structural stability, thereby increasing the quality factor ($Q \times f$) and minimizing dielectric loss. High-entropy ceramic $(Nd_{0.2}Eu_{0.2}Y_{0.2}Ho_{0.2}Yb_{0.2})VO_4$, featuring a tetragonal zircon structure with space group $I4_1/amd$, was synthesized via the conventional solid-state reaction method. The $(Nd_{0.2}Eu_{0.2}Y_{0.2}Ho_{0.2}Yb_{0.2})VO_4$ high-entropy ceramics exhibited a low dielectric constant of $\varepsilon_r = 11.55$ and a negative temperature coefficient of the resonant frequency ($\tau_f = -37.3$ ppm/°C), and it can be combined with TiO_2 to obtain a near-zero τ_f of −2.4 ppm/°C. $(Nd_{0.2}Eu_{0.2}Y_{0.2}Ho_{0.2}Yb_{0.2})VO_4$ featured a high quality factor ($Q \times f$ = 76,400 GHz) at 12.31 GHz, which exceeded that of conventional zircon ceramics by more than twofold, representing the highest reported $Q \times f$ value for vanadium-based zircon ceramics to date. The $(Nd_{0.2}Eu_{0.2}Y_{0.2}Ho_{0.2}Yb_{0.2})VO_4$ high-entropy ceramics with a zircon structure, which exhibited excellent comprehensive dielectric properties, is anticipated to possess substantial application potential in high-performance and high-power microwave devices.

Acknowledgements

This work was supported by the Natural Science Foundation of Guangxi Zhuang Autonomous Region (No. 2023GXNSFBA026076), the Science and Technology Plan of Guangxi (No. ZY22096019), and the National Natural Science Foundation of China (No. 52462016). We thank the administrators at the IR beamline workstation (BL01B) of the National Synchrotron Radiation Laboratory (NSRL) for their help in the IR measurement and fitting.

Declaration of competing interest

The authors have no competing interests to declare that are relevant to the content of this article.

References

[1] Yin CZ, Yin YH, Du K, *et al.* Fabrication of high-efficiency dielectric patch antennas from temperature-stable $Sr_{3-x}Ca_xV_2O_8$ microwave dielectric ceramic. *J Eur Ceram Soc* 2023, **43**: 1492–1499.

[2] Bao J, Zhang YP, Kimura H, *et al.* Crystal structure, chemical bond characteristics, infrared reflection spectrum, and microwave dielectric properties of $Nd_2(Zr_{1-x}Ti_x)_3(MoO_4)_9$ ceramics. *J Adv Ceram* 2023, **12**: 82–92.

[3] Xiang HC, Kilpijärvi J, Myllymäki S, *et al.* Spinel-olivine microwave dielectric ceramics with low sintering temperature and high quality factor for 5 GHz Wi-Fi antennas. *Appl Mater Today* 2020, **21**: 100826.

[4] Wu FF, Zhou D, Du C, *et al.* Design of a sub-6 GHz dielectric resonator antenna with novel temperature-stabilized $(Sm_{1-x}Bi_x)NbO_4$ (x = 0–0.15) microwave dielectric ceramics. *ACS Appl Mater Inter* 2022, **14**: 7030–7038.

[5] Sebastian MT, Ubic R, Jantunen H. Low-loss dielectric ceramic materials and their properties. *Int Mater Rev* 2015, **60**: 392–412.

[6] Wang X, Zhu XL, Li L, *et al.* Structure evolution and adjustment of τ_f in (Ba,Sr)HfO_3 and (Sr,Ca)HfO_3 microwave dielectric ceramics. *J Am Ceram Soc* 2024, **107**: 285–299.

[7] Mohanty P, Keshri S, Sinha M K, *et al.* Study on microwave dielectric properties of corundum type $(Mg_{1-x}Co_x)_4Ta_2O_9$ (x = 0–0.6) ceramics for designing a microwave low pass filter. *Ceram Int* 2016, **42**: 5911–5920.

[8] Tang Y, Zhang ZW, Li J, *et al.* $A_3Y_2Ge_3O_{12}$ (A = Ca, Mg): Two novel microwave dielectric ceramics with contrasting τ_f and $Q \times f$. *J Eur Ceram Soc* 2020, **40**: 3989–3995.

[9] Zhang N, Chen JQ, Zhang YH, *et al.* Crystal structure, bond characterization and lattice energy of B-site 1:3 ordering inverse spinel $Li_{1.25}Ga_{0.25}Ti_{1.5}O_4$ ceramic. *Ceram Int* 2024, **50**: 126–133.

[10] Liu K, Zhang HW, Liu C, *et al.* Crystal structure and microwave dielectric properties of $(Mg_{0.2}Ni_{0.2}Zn_{0.2}Co_{0.2}Mn_{0.2})_2SiO_4$—A novel high-entropy ceramic. *Ceram Int* 2022, **48**: 23307–23313.

[11] Yao Y, Wang Y, Bafrooei HB, *et al.* Ni–Co complex ionic synergistically modifying octahedron lattice of cordierite ceramics for the application of 5G microwave-millimeter-wave antennas. *Inorg Chem* 2024, **63**: 10022–10030.

[12] Song ZJ, Song KX, Liu B, *et al.* Temperature-dependent dielectric and Raman spectra and microwave dielectric properties of gehlenite-type $Ca_2Al_2SiO_7$ ceramics. *Int J Appl Ceram Tec* 2020, **17**: 771–777.

[13] Wang G, Li ZP, Xiong G, *et al.* A novel $Ba_4(La_{1/5}Pr_{1/5}Nd_{1/5}Sm_{1/5}Eu_{1/5})_{28/3}Ti_{18}O_{54}$ high-entropy microwave dielectric ceramic with tungsten bronze-type and high-permittivity. *Mater Today Commun* 2024, **40**: 109855.

[14] Guo HH, Zhou D, Liu WF, *et al.* Microwave dielectric properties of temperature-stable zircon-type (Bi,Ce)VO_4 solid solution ceramics. *J Am Ceram Soc* 2020, **103**: 423–431.

[15] Xiang HC, Zhang YH, Chen JQ, *et al.* Structure evolution and τ_f influence mechanism of $Bi_{1-x}HoVO_4$ microwave dielectric ceramics for LTCC applications. *J Mater Sci Technol* 2024, **197**: 1–8.

[16] Li W, Fang L, Sun YH, *et al.* Preparation, crystal structure and microwave dielectric properties of rare-earth vanadates: $ReVO_4$ (Re = Nd, Sm). *J Electron Mater* 2017, **46**: 1956–1962.

[17] Dai YM, Chen JW, Tang Y, *et al.* Relationship between bond characteristics and microwave dielectric properties of $REVO_4$ (RE = Yb, Ho) ceramics. *Ceram Int* 2023, **49**: 875–881.

[18] Yeh JW, Chen SK, Lin SJ, *et al.* Nanostructured high-entropy alloys with multiple principal elements: Novel alloy design concepts and outcomes. *Adv Eng Mater* 2004, **6**: 299–303.

[19] Jiao YT, Dai J, Fan ZH, *et al.* Overview of high-entropy oxide ceramics. *Mater Today* 2024, **77**: 92–117.

[20] Xie MJ, Lai YM, Xiang PW, *et al.* The entropy effect on the structure and microwave dielectric properties of high-entropy $Li_x(MgZnCoNi)_{(1-x)/4}Al_2O_{4-\delta}$ ceramics. *Chem Eng J* 2024, **496**: 154132.

[21] Zhang M, Xu XZ, Ahmed S, *et al.* Phase transformations in an Aurivillius layer structured ferroelectric designed using the high entropy concept. *Acta Mater* 2022, **229**: 117815.

[22] Xiang HC, Yao L, Chen JQ, *et al.* Microwave dielectric high-entropy ceramic $Li(Gd_{0.2}Ho_{0.2}Er_{0.2}Yb_{0.2}Lu_{0.2})GeO_4$ with stable temperature coefficient for low-temperature cofired ceramic technologies. *J Mater Sci Technol* 2021, **93**: 28–32.

[23] Lin FL, Liu B, Zhou QW, *et al.* Novel non-equimolar $SrLa(Al_{0.25}Zn_{0.125}Mg_{0.125}Ga_{0.25}Ti_{0.25})O_4$ high-entropy ceramics with excellent mechanical and microwave dielectric properties. *J Eur Ceram Soc* 2023, **43**: 6909–6915.

[24] Lin FL, Liu B, Hu CC, *et al.* Novel high-entropy microwave dielectric ceramics $Sr(La_{0.2}Nd_{0.2}Sm_{0.2}Eu_{0.2}Gd_{0.2})AlO_4$ with excellent temperature stability and mechanical properties. *J Eur Ceram Soc* 2023, **43**: 2506–2512.

[25] Yao Y, Cao L, Yang HY, *et al.* High-entropy $Mg_{1.8}R_{0.2}Al_4Si_5O_{18}$ (R = Ni, Co, Zn, Cu, Mn) cordierite ceramics: Influence of octahedral distortion and electronegativity mismatch on the microwave dielectric properties. *Ceram Int* 2024, **50**: 51826–51831.

[26] Chakoumakos BC, Abraham MM, Boatner LA. Crystal structure refinements of zircon-type MVO_4 (M = Sc, Y, Ce, Pr, Nd, Tb, Ho, Er, Tm, Yb, Lu). *J Solid State Chem* 1994, **109**: 197–202.

[27] Gong JB, Fan XD, Dai RC, *et al.* High-pressure phase transition of micro- and nanoscale $HoVO_4$ and high-pressure phase diagram of $REVO_4$ with RE ionic radius. *ACS Omega* 2018, **3**: 18227–18233.

[28] Santos CC, Silva EN, Ayala AP, *et al.* Raman investigations of rare earth orthovanadates. *J Appl Phys* 2007, **101**: 053511.

[29] Wu FF, Zhou D, Du C, *et al.* A comprehensive study on crystal structure, phase compositions of the $BiVO_4$–$LaVO_4$ binary dielectric

ceramic system and a typical design of dielectric resonator antenna for C-band applications. *Appl Mater Today* 2024, **38**: 102222.
[30] Roberts AC, Burns PC, Gault RA, *et al.* Paganoite, $NiBi^{3+}As^{5+}O_5$, a new mineral from Johanngeorgenstadt, Saxony, Germany: Description and crystal structure. *Eur J Mineral* 2001, **13**: 167–175.
[31] Zhao B, Yan ZK, Du YQ, *et al.* High-entropy enhanced microwave attenuation in titanate perovskites. *Adv Mater* 2023, **35**: 2210243.
[32] Liu M, Xu ZT. Micromechanical characterization of microwave dielectric ceramic $BaO–Sm_2O_3–5TiO_2$ by indentation and scratch methods. *J Adv Ceram* 2023, **12**: 1136–1165.
[33] Shannon RD. Dielectric polarizabilities of ions in oxides and fluorides. *J Appl Phys* 1993, **73**: 348–366.
[34] Rysselberghe PV. Remarks concerning the Clausius–Mossotti law. *J Phys Chem* 1932, **36**: 1152–1155.
[35] Shannon RD, Rossman GR. Dielectric constant of $MgAl_2O_4$ spinel and the oxide additivity rule. *J Phys Chem Solids* 1991, **52**: 1055–1059.
[36] Tang L, Yang HC, Li EZ, *et al.* A novel $Na_{1-x}K_xTaO_3$ perovskite microwave dielectric ceramic with high permittivity and high positive temperature coefficient. *J Adv Ceram* 2023, **12**: 2053–2061.
[37] Xiang HC, Li CC, Jantunen H, *et al.* Ultralow loss $CaMgGeO_4$ microwave dielectric ceramic and its chemical compatibility with silver electrodes for low-temperature cofired ceramic applications. *ACS Sustain Chem Eng* 2018, **6**: 6458–6466.
[38] Li C, Hou JL, Ye ZJ, *et al.* Lattice occupying sites and microwave dielectric properties of $Mg^{2+}–Si^{4+}$ co-doped $Mg_xY_{3-x}Al_{5-x}Si_xO_{12}$ garnet typed ceramics. *J Mater Sci Mater El* 2022, **33**: 2116–2124.
[39] Li JM, Wang ZX, Guo YF, *et al.* Influences of substituting of $(Ni_{1/3}Nb_{2/3})^{4+}$ for Ti^{4+} on the phase compositions, microstructures, and dielectric properties of $Li_2Zn[Ti_{1-x}(Ni_{1/3}Nb_{2/3})_x]_3O_8$ ($0 \le x \le 0.3$) microwave ceramics. *J Adv Ceram* 2023, **12**: 760–777.
[40] Lyu XS, Li LX, Zhang S, *et al.* A new low-loss dielectric material $ZnZrTa_2O_8$ for microwave devices. *J Eur Ceram Soc* 2016, **36**: 931–935.
[41] Wu FF, Zhou D, Xia S, *et al.* Low sintering temperature, temperature-stable scheelite structured $BiV_{1-x}(Fe_{1/3}W_{2/3})_xO_4$ microwave dielectric ceramics. *J Eur Ceram Soc* 2022, **42**: 5731–5737.
[42] Kamba S, Wang H, Berta M, *et al.* Correlation between infrared, THz and microwave dielectric properties of vanadium doped antiferroelectric $BiNbO_4$. *J Eur Ceram Soc* 2006, **26**: 2861–2865.
[43] Wakino K, Murata M, Tamura H. Far infrared reflection spectra of B a(Zn,Ta)$O_3–BaZrO_3$ dielectric resonator material. *J Am Ceram Soc* 1986, **69**: 34–37.
[44] Yang HY, Zhang SR, Yang HC, *et al.* Intrinsic dielectric properties of columbite $ZnNb_2O_6$ ceramics studied by P–V–L bond theory and Infrared spectroscopy. *J Am Ceram Soc* 2019, **102**: 5365–5374.
[45] Wu ZJ, Meng QB, Zhang SY. Semiempirical study on the valences of Cu and bond covalency in $Y_{1-x}Ca_xBa_2Cu_3O_{6+y}$. *Phys Rev B* 1998, **58**: 958–962.
[46] Du QB, Tang Y, Li J, *et al.* A low-ε_r and high-Q microwave dielectric ceramic Li_2SrSiO_4 with abnormally low sintering temperature. *J Eur Ceram Soc* 2021, **41**: 7678–7682.
[47] Zhou X, Liu LT, Sun JJ, *et al.* Effects of $(Mg_{1/3}Sb_{2/3})^{4+}$ substitution on the structure and microwave dielectric properties of $Ce_2Zr_3(MoO_4)_9$ ceramics. *J Adv Ceram* 2021, **10**: 778–789.
[48] Tian CY, Wang FF, Ye X, *et al.* Bipolar fatigue-resistant behavior in ternary $Bi_{0.5}Na_{0.5}TiO_3–BaTiO_3–SrTiO_3$ solid solutions. *Scripta Mater* 2014, **83**: 25–28.
[49] Kumar N, Cann DP. Electromechanical strain and bipolar fatigue in $Bi(Mg_{1/2}Ti_{1/2})O_3–(Bi_{1/2}K_{1/2})TiO_3–(Bi_{1/2}Na_{1/2})TiO_3$ ceramics. *J Appl Phys* 2013, **114**: 13687–13796.
[50] Deng JM, Liu LJ, Sun XJ, *et al.* Dielectric relaxation behavior and mechanism of $Y_{2/3}Cu_3Ti_4O_{12}$ ceramic. *Mater Res Bull* 2017, **88**: 320–329.
[51] Shi T, Zhang F, Sun WY, *et al.* Fabrication, sinterability and microwave dielectric properties of $MgTiO_3–(Ca_{0.8}Sr_{0.2})TiO_3$ composite ceramics from nanosized powders. *Vacuum* 2022, **201**: 111107.
[52] Zhang A, Fan HQ, Yang F, *et al.* Defects evolution and temperature stability of low-loss magnesium titanate stannate-calcium strontium titanate microwave dielectric ceramics. *J Alloys Compd* 2022, **925**: 166633.